On the formation and stability of disks in binaries with intermediate separations

M. Huarte-Espinosa[1], J. Carroll-Nellenback[1], J. Nordhaus[1,2], A. Frank[1] and E. G. Blackman[1]

Received ____________; accepted ____________

[1]Department of Physics and Astronomy, University of Rochester, 600 Wilson Boulevard, Rochester, NY, 14627-0171

[2]RIT...

ABSTRACT

Subject headings: ? — ? — ? —

1. Introduction

The process of accretion from a primary wind onto a secondary star is a specific case of Bondi-Hoyle-Lyttleton (BHL) accretion (e.g. Edgar 2004 for a review) and is observed to play a direct role in the phenomenology of some asymmetric PPN (the best studied example is the Red Rectangle; Witt et al. 2009). Disk formation around the secondary via AGB wind capture was first studied computationally with SPH calculations 14 years ago (Mastrodemos & Morris 1998), then by Podsiadlowski & Mohamed (2007) using GADGET, and more recent 2D FLASH simulations of BHL accretion were performed by de Val-Borro et al. (2009). These studies found signicant enhancements over BHL accretion rates onto the secondary. Such result however must be tested in 3- D using high resolution simulations because the implications for the maximum outflow (jet) power are dramatic; the answer could rule in, or out, the secondary as the engine powering jets in pot-AGB stars and Young Stellar Objects (YSO).

1.1. Bondi-Hoyle accretion onto a moving object (impact parameter)

The BHL accretion occurs when a compact object of mass, m, moves at a constant supersonic velocity, v_w, though an infinite gas cloud which is homogeneous at infinity. The gravitational field of m focuses the cloud material located within the BHL radius

$$r_b = 2Gm/v_w \tag{1}$$

into a wake. A conical shock is formed and divides the wake into (i) material that is accreted (ii) material that flows away from the object. These flow components are separated by a stagnation point (Bondi & Hoyle, 1944).

Here we study a system in which the cloud material is that of an AGB star's wind, tens of AU away from the stellar center, with a terminal speed v_w. The accretor is an orbiting companion of mass, $m = m_s$, which has a constant acceleration that points towards the primary. The wake that develops under these conditions is not aimed towards the instantaneous position of the companion as in the BHL accretion. Instead, the wake aims towards a point between the companion's original and current positions; the focused material is accelerated on average towards a retarded position. The time-scale associated with this wind capture process scales up with r_b/v_w. Thus the distancei, I, that a volume of gas, dv, has moved due to this acceleration is

$$I = 1/2 a_c t^2 \cos\alpha, \tag{2}$$

where α is the angle between $\mathbf{v_w}$ and the acceleration vector. We call I "the impact parameter".

In an inertial reference frame that co-rotates with the secondary at t_0, the companion accelerates towards the primary at $r_s\Omega^2$. The projection of this relative to the incoming flow velocity is then

$$r_s\Omega^2 \frac{v_s}{\sqrt{v_s^2 + v_w^2}}. \tag{3}$$

Given that acceleration of the captured material occurs during a time scale

$$\frac{r_b}{\sqrt{v_s^2 + v_w^2}}, \tag{4}$$

the offset scales up with

$$\frac{v_s^3 r_b^2}{2r_s(v_s^2 + v_w^2)^{3/2}}\hat{\mathbf{r}}. \tag{5}$$

This implies the wake, or "backflow", returns at some small distance from the secondary and will then proceed into a prograde orbit about the secondary. In summary, I falls off with the orbital radius supporting the fact that disks start small (section 3).

2. Model and initial set-up

We model the formation and evolution of disks which are formed in binaries due to wind capture. We solve the equations of hydrodynamics in three-dimensions. In non-dimensional conservative form, these are given by

$$\frac{\partial \rho}{\partial t} + \nabla \cdot (\rho \mathbf{v}) = 0 \tag{6}$$

$$\frac{\partial \mathbf{v}}{\partial t} + (\mathbf{v} \cdot \nabla)\mathbf{v} = -\frac{1}{\rho}\nabla p - \Phi \tag{7}$$

where ρ, p and $\mathbf{v}$ are the gas density, thermal pressure and flow velocity, respectively. We use an isothermal equation of state, thus $\gamma = 1$. In (7)

$$\Phi = \begin{cases} -\frac{Gm_s}{\sqrt{r}}, & \text{for } r > 4dr; \\ -\frac{Gm_s}{\sqrt{4dr}}, & \text{for } r \leq 4dr. \end{cases} \tag{8}$$

where $4dr = 4\sqrt{dx^2 + dy^2 + dz^2}$ is the softening radius.

We solve these equations using the adaptive mesh refinement (AMR) numerical code *AstroBEAR2.0*[1] which uses a single step, second-order accurate, shock capturing scheme (Cunningham et al. 2009; Carroll-Nellenback et al. 2011). While AstroBEAR2.0 is able to compute several microphysical processes such as gas self-gravity and heat conduction, we do not consider these in the present study.

[1]https://clover.pas.rochester.edu/trac/astrobear/wiki

2.1. Grid

We use cubic or box-like computational domains with volumes $(1.6r_b)^3$ or $1.6^2{\times}0.8r_b^3$, respectively. Wind boundary conditions (section 2.2.1) were set at the $-x, +y$ and $\pm z$ domain faces, while outflow only conditions were set at all other faces. The positions of the primary, the center of mass and the secondary are ($-r_p$,0,0), (0,0,0), and (r_s,0,0), respectively. We use a reference frame which co-rotates with the secondary, thus Coriolis terms are included in (7).

The grid consisted of nested cell blocks with decreasing cell size, by factors of a half, and centered at the secondary's position. These cell blocks had the same geometry as the grid. The innermost block has a width of $\sim$64–80 finest cells. We had used very similar grid distributions in all our simulations. Grid resolution as well as other relevant model parameters are shown in table 1.

We use *BlueHive*[2] –an IBM massively parallel processing supercomputer of the Center for Integrated Research Computing of the University of Rochester– and *Ranger*[3] –a Sun Constellation Linux Cluster which is part of the TeraGrid project– to run simulations for an average running time of about

?

day/orbit using 64–512 processors.

---

[2]https://www.rochester.edu/its/web/wiki/crc/index.php/ Systems#Blue_Gene.2FP

[3]https://www.xsede.org/web/guest/tacc-ranger

2.2. Initial conditions

We model the primary as an AGB star with a mass of $1.5\,\mathrm{M}_{\odot}$, a spherical constant wind with a terminal speed $v_w = 10\,\mathrm{km\,s^{-1}}$ and a mass-loss of $\dot{M} = 10^{-5}\,M_{\odot}\,\mathrm{yr}^{-1}$. The secondary is implemented with a sink particle **BASED ON THE IMPLEMENTATION OF REF...** and models a main sequence star, or a white dwarf, with $1\,\mathrm{M}_{\odot}$ in a circular orbit about the primary.

2.2.1. Wind solution

For the initial conditions we set all grid cells with the wind solution. This has a constant temperature of 1000 K and a density given by

$$\frac{\dot{m}_p}{4\pi(\mathbf{x}_p - \mathbf{x})^2 v_w}, \tag{9}$$

where $\mathbf{x}_p$ and $\mathbf{x}$ are the positions of primary's orbit and that of an arbitrary grid cell, respectively, relative to the centrer of mass (0,0,0).

We calculate the velocity field of the solution by solving for the characteristics that leave the surface of the primary at a *retarded* time, $t_r = t - |\mathbf{x}|/v_w$, with a velocity vector pointing towards $\mathbf{x}$. Wind speeds are chosen so that $v_w > |\mathbf{v}_s|$, where $\mathbf{v}_s$ is the secondary's orbital velocity. We assume that the distance from the primary's surface to $\mathbf{x}$ is larger than $|\mathbf{x}_p|$, which constraints the separation between the secondary and the grid's boundaries. As time goes from t_r to t the primary covers a circular segment of radius r_p starting at $\mathbf{x}_p(t_r)$, with a displacement vector $\mathbf{d} = \mathbf{x} - \mathbf{x}_p(t_r)$. We calculate the wind normal, $\hat{\mathbf{n}}$, so that $(v_w\hat{\mathbf{n}} + \mathbf{v}_p(t_r)) \times \mathbf{d} = 0$. Starting at the primary's surface, the wind velocity is then

$$\mathbf{v}_w = v_w\hat{\mathbf{n}} + \mathbf{V}_p(t_r), \tag{10}$$

which yields a better approximation of the retarded time

$$\tau_r = t - |\mathbf{x}|/|\mathbf{v}|. \tag{11}$$

We iterate the above computations until we find a convergent wind solution for the gird cell located at $\mathbf{x}$. Finally we switch to a reference frame that co-rotates with the secondary.

2.3. Wind injection

We continually set the above wind solution in the grid cells of the $-x, +y$ and $\pm z$ domain faces. For each iteration however we use $\tau, \mathbf{x}_p(\tau)$ and $\mathbf{v}$ as initial conditions in a recursive Runge-Kutta method to calculate the deflection of $\mathbf{v}$ caused by the secondary's gravity field, as it travels from the primary's surface ($\sim\ x_p(\tau)$) to $\mathbf{x}$. We consider the orbital motion of the secondary in these computations. This step yields yet better estimates of $\hat{\mathbf{n}}$ and τ than the calculations in section 2.2.1 alone. We therefore use the new values of $\hat{\mathbf{n}}$ and τ for the next iteration of the wind solution (above).

Finally, to match the initial conditions and the injected wind solution we allow the gravitational effect of the secondary on the gas to increase linearly during one wind crossing time, $1.6 r_b/v_w$, from zero to Gm_s/r. The field remains constant thereafter. This has no effect on the binary orbital motion.

2.4. Simulations

We carry out three simulations corresponding to stellar separation of 10, 15 and 20 AU. Table 1 summarizes the models and their relevant parameters.

3. Results

3.1. Disk formation and structure

Table 1. Simulations and parameters.

Name	Separation [AU]	Resolution	r_b [AU]
M1	10	64x64x32+2amr	4.9
M3	20	64x64x32+4amr	6.3

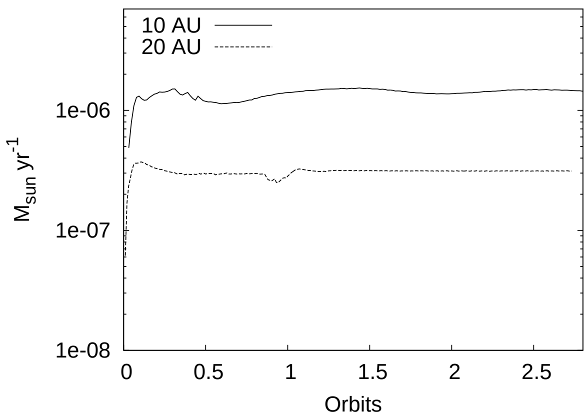

Fig. 1.— Secondary (particle) accretion rate evolution.

In Figure 1 we show the evolution of the secondary's (particle) accretion rate. We consistently see an initial very fast and brief increase, followed by a mild short decrease and then the profiles remain almost flat. The position of the brief small dip in the 20 AU profile corresponds to the moment in which the disk is formed. The accretion rates that we find are higher than those obtained in previous binary wind capture models (see Section 4).

WILL MOVE THIS PARAGRAPH TO "DISCUSSION" SECTION BELOW: The secondary accretion rates that we find in our simulations are higher than those reported by de Val-Borro et al. (2009, see their table 3), who, e.g., report $\dot{M}_{acc}/\dot{M}_{wind}$ ~0.06 after 2 orbits for a 70 AU case. This was expected since we have followed wind capture and accretion in 3-D, whereas de Val-Borro et al. (2009) followed these processes in 2-D, hence no polar accretion. However, the gradients of their accretion rate profiles (de Val-Borro et al. 2009, their Fig. 12) are similar to ours (Figure 1): a very fast and brief initial increase followed by rather mild variations. Moreover, the values of $\dot{m}$ that we find are also higher than those predicted by the semi-analytic models of Perets & Kenyon (2012).

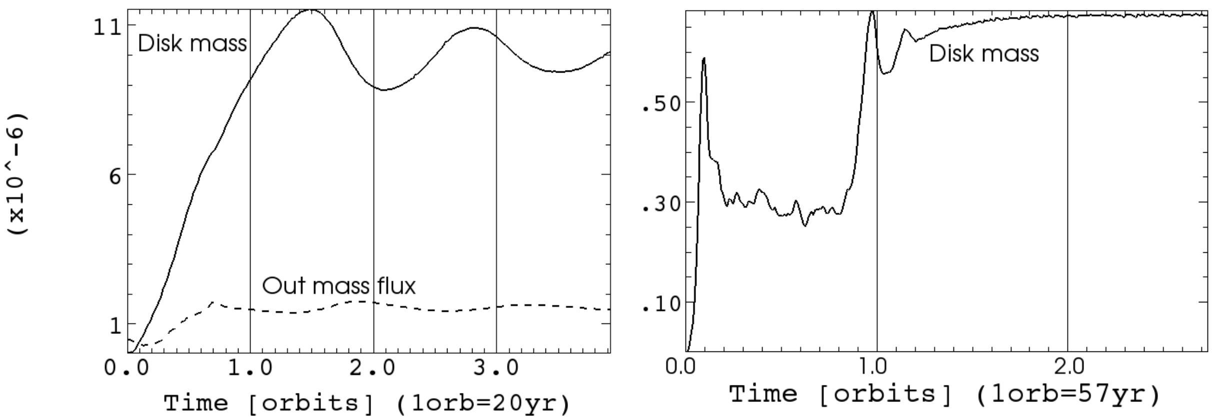

(a) a = 10 AU *(b) a = 20 AU*

Fig. 2.— Disk mass as a function of time [$M_\odot$] (solid) and flux of gas that leaves the grid [$M_\odot\,yr^{-1}$] (dashed).

In Figure 2 we show profiles of the disks' mass (solid lines) as a function of time and binary separation. These are calculated by adding the mass of grid cells which contain bound gas (the gravitational energy is greater than the kinetic one).

In the 10 AU case we see that the mass increases for 1.5 orbits and reaches a maximum value of 1.1×10^{-5} $M_\odot$. The profile then oscillates with a wavelength of $\sim$1 orbit and an amplitude which has a maximum initial value of about 20% but decreases in time. The disk's mass will then converge to $\sim 10^{-5}\,M_\odot$. To understand the origin of the disk mass oscillations we have also calculated the flux of gas that leaves the grid (dashed line). The position and shape of the gradients in both the solid and dashed lines show that the disk's mass decreases at the same time as the flux of gas away form the grid increases, and that the disk's mass increases when the flux of gas away form the grid decreases. This suggests that the wind's ram pressure is able to strip a small yet significant fraction of disk gas during its early evolutionary phases.

The disk mass profile of the 20 AU model is quite different. It shows some initial mass corresponding to gas which ends up been accreted onto the particle. Yet the disk forms at $t \approx 0.85$ orbits. At this point the disk's mass increases very fast, in a matter of 5.5 yr, and reaches a maximum value of $\sim 6.5 \times 10^{-7}\,\mathrm{M}_{\odot}$. Then, after a brief relaxation period the disk mass profile converges to $\sim 6.5 \times 10^{-7}\,\mathrm{M}_{\odot}$. We do not see any disk mass oscillations related to wind stripping as in the 10 AU model, likely because the wind's ram pressure is weaker by a factor of 0.5.

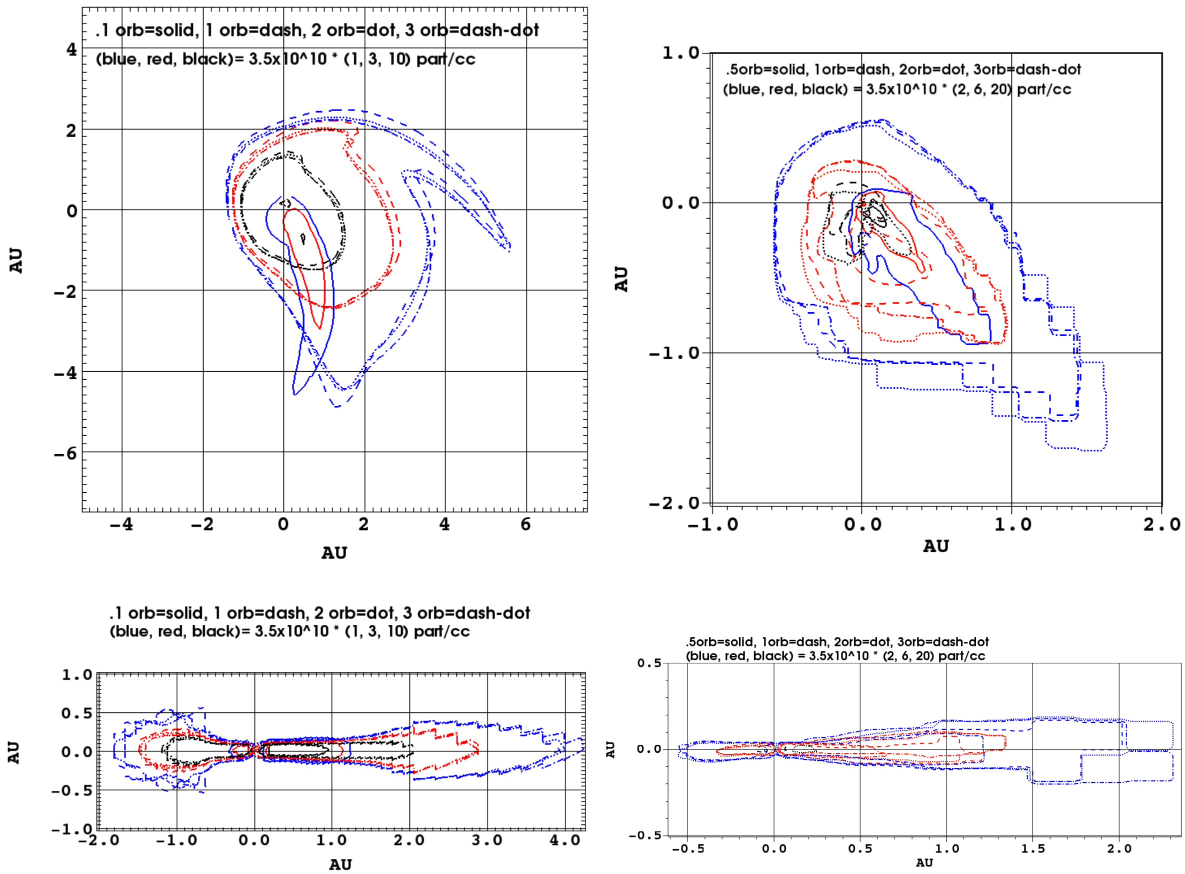

Fig. 3.— Disk density structure at 4 times. Top: orbital plane view. Bottom: longitudinal plane view. Left: 10 AU model. Right: 20 AU model.

In Figure 3 we show logarithmic density contours on slices though the orbital plane (up) and though a longitudinal plane aligned with the wind's inflow direction. Each panel has 12 contours arranged by line type and color: blue, red and black represent densities of 3.5, 10.5 and $35{\times}10^{10}$ part cm^{-3}, respectively. Dashed, dotted and dashed-dotted lines represent densities at $t = 1$, 2 and 3 orbits, respectively.

By comparing same color lines in these density contour maps (Figure 3) we see that the structure of the disks changes only mildly after they form ($t > 1$ orb). Disks are thin, not symmetric and have a flared vertical structure. We find that the steepest density gradients are located in the disks' part facing the incoming wind (top left region in top panels and left region in bottom panels), and that both the disks' radius and edge height are inversely proportional to a. Thus the shape of the orbits of disk gas is a function of a (section 4.1).

In addition to disk density contours (above), in Figures 5 and 6 we present logarithmic density gray-scale maps of the gas on the orbital plane and on the longitudinal plane which is aligned with the wind's inflow direction at $t = 1$, 2 and 3 orbits.

4. Discussion

4.1. Disk gas orbits

The shape of the orbits strongly depends on a. $\epsilon \propto a^{\beta}$.

4.2. Grid resolution

Accretion disk simulations are known to be affected by grid resolution. To assess this matter we have carried out additional runs of our simulations (see Table 1) but with slight resolution variations. For the 10 AU case we independently tried (1) a lower grid resolution of 64^3 cells (four times smaller that in Model 1) and (2) increasing the volume of the central box of finest cells around the particle (section 2.2) from $(r_b/4)^3$ (Model 1) to $(r_b/2)^3$. Only the small scale features of the disks show differences.

5. CONCLUSIONS

Financial support for this project was provided by the Space Telescope Science Institute grants HST-AR-11251.01-A and HST-AR-12128.01-A; by the National Science Foundation under award AST-0807363; by the Department of Energy under award DE-SC0001063; and by Cornell University grant 41843-7012. This work used the Extreme Science and Engineering Discovery Environment (XSEDE), which is supported by National Science Foundation grant number OCI-1053575.

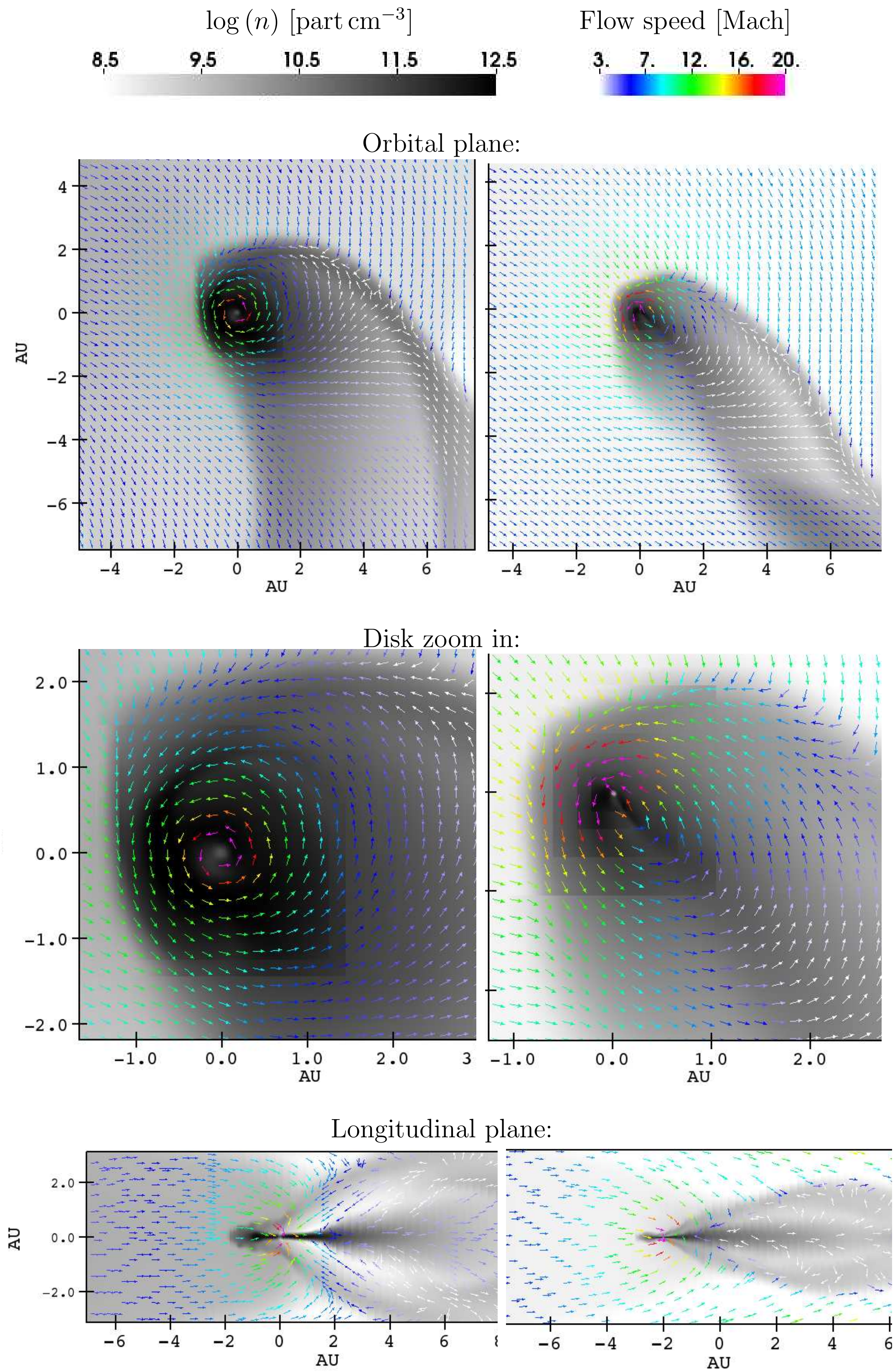

Fig. 4.— From left to right panels correspond to 1, 2 and 3 binary orbits.

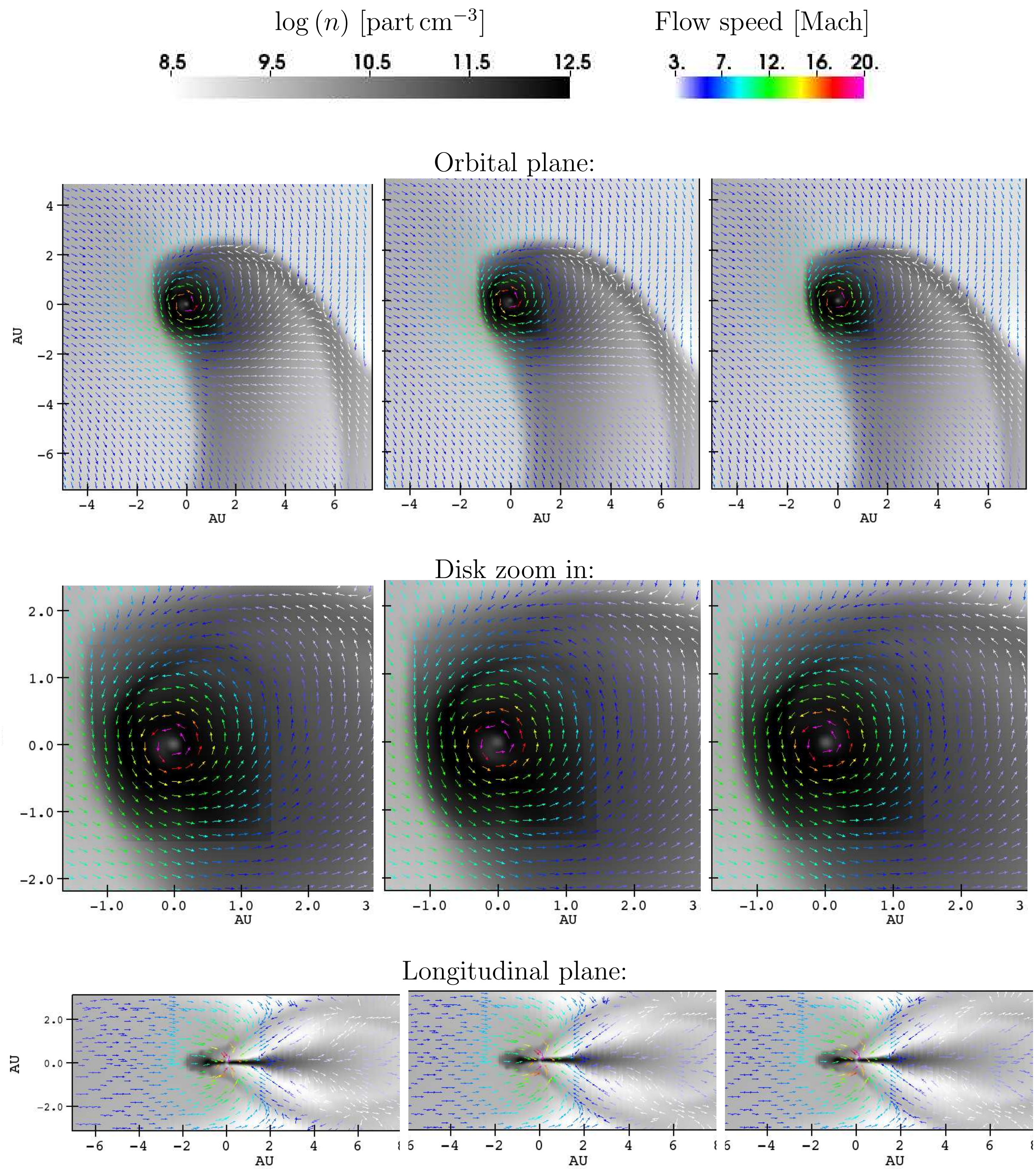

Fig. 5.— Structure and evolution of the gas in Model 1 ($a = 10\,\mathrm{AU}$). From left to right panels correspond to 1, 2 and 3 binary orbits.

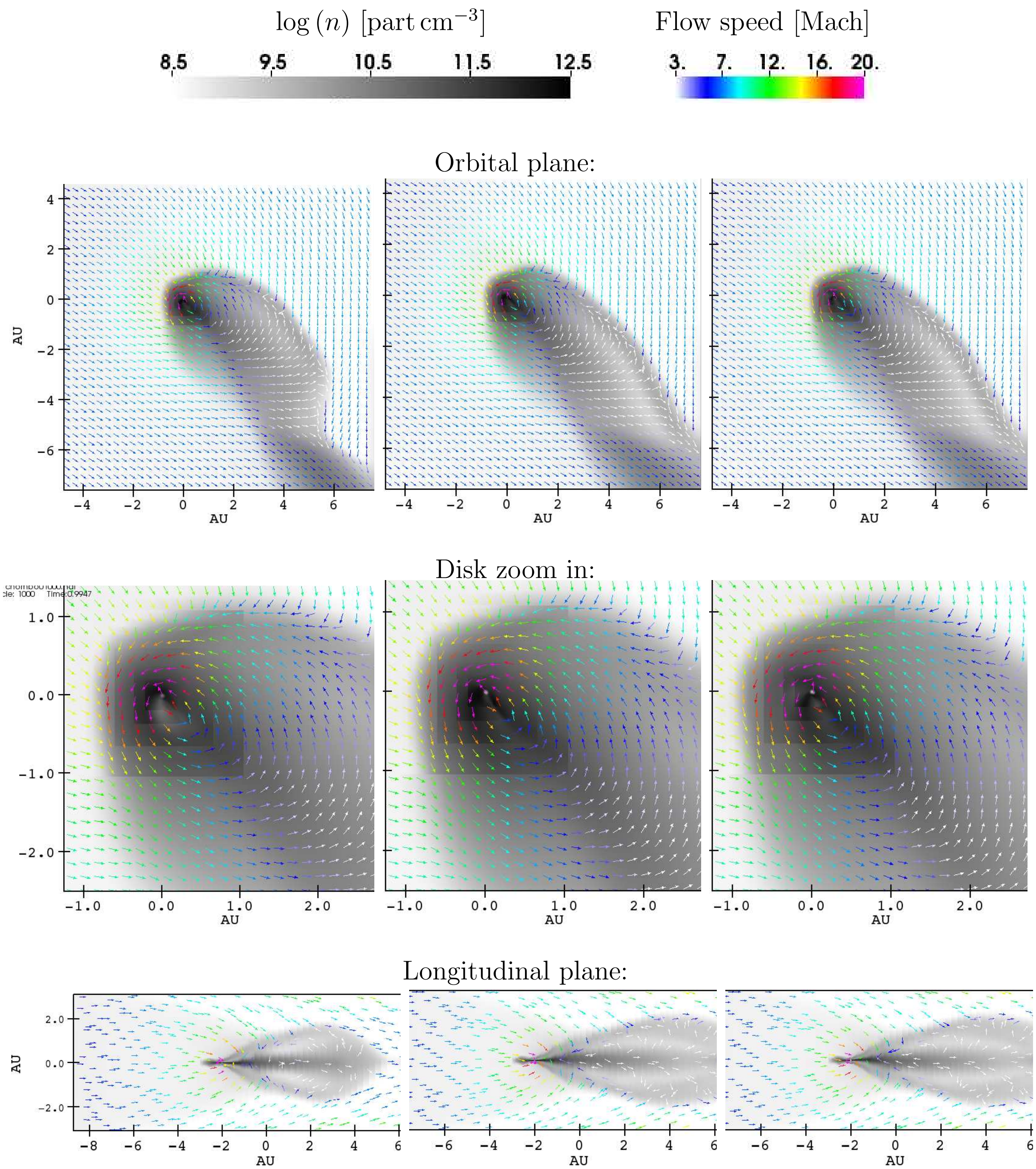

Fig. 6.— Structure and evolution of the gas in Model 1 ($a = 20\,\mathrm{AU}$). From left to right panels correspond to 1, 2 and 3 binary orbits.

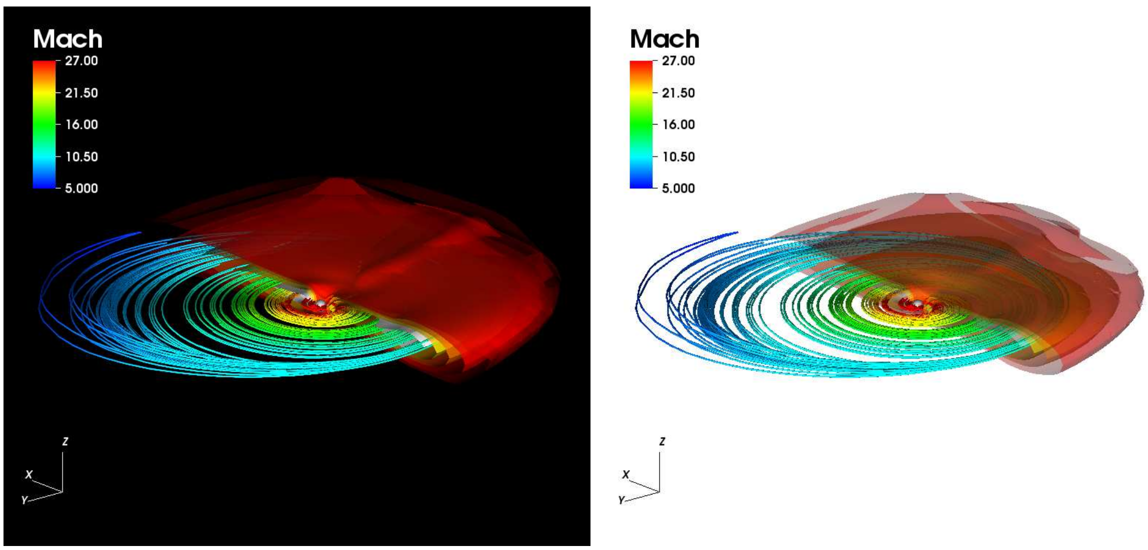

VERSION 1 VERSION 2

Fig. 7.— Disk gas orbit streamlines and density contours for the 10 AU case after 2 orbits. The central white small sphere is the secondary's particle. The wind enters the grid towards the image. Streamline colors denote orbital speed in Mach units.

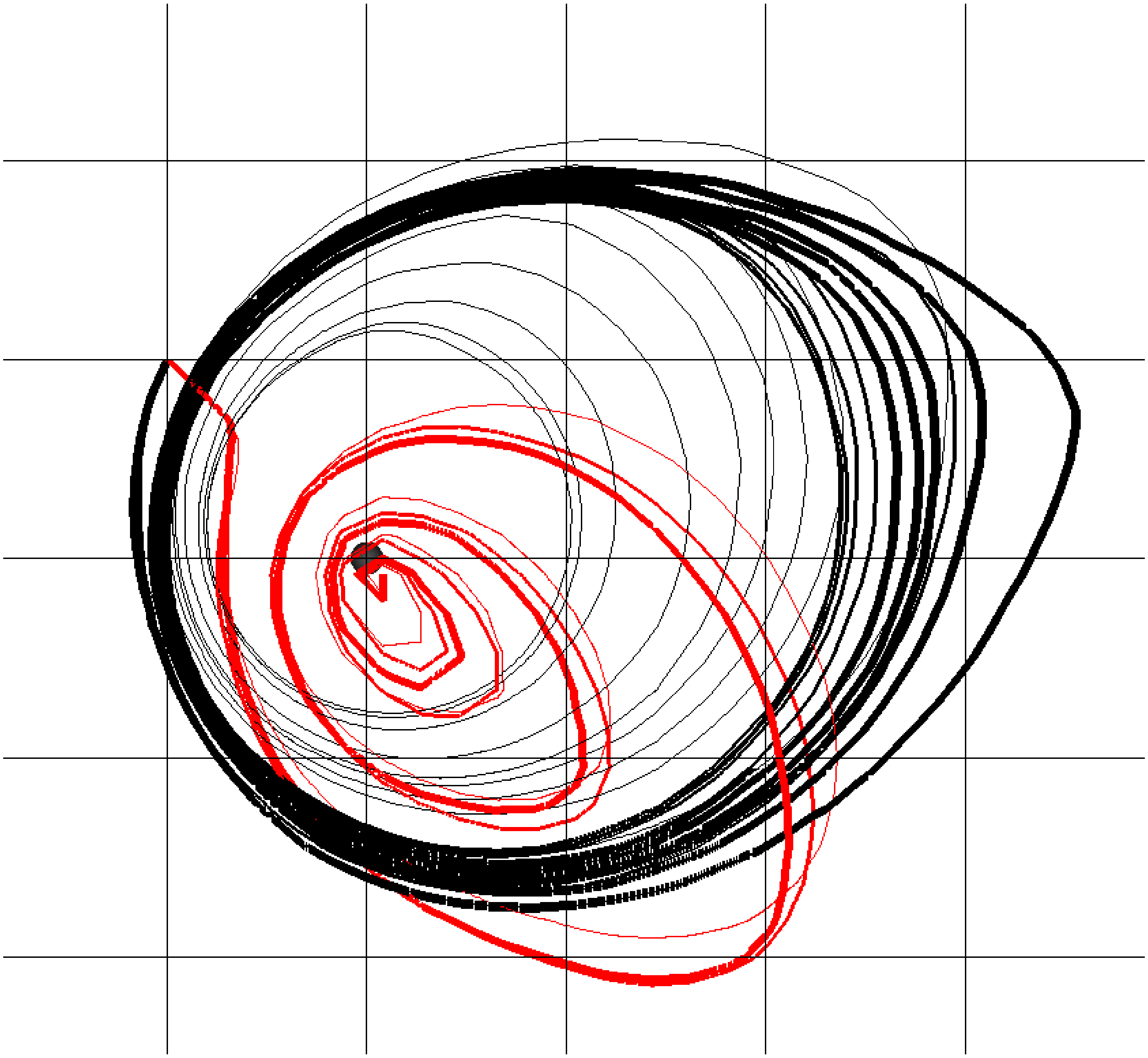

Fig. 8.— Disk orbit streamlines, comparison at 3 times: 1 orb=thin; 2 orb=thicker; 3 orb=thickest, orbital plane view. 10 AU model in black and 20 AU model in red. Grid squares are 1 AU^2. The wind enters the grid from the top left corner at angles close to 45°.

REFERENCES

Blackman, E. G., Frank, A., & Welch, C. 2001, ApJ, 546, 288

Blackman E.G., 2007, Ap&SS, 307, 7

Blandford, R. D., & Payne, D. G. 1982, MNRAS, 199, 883

Carroll-Nellenback, J. J., Shroyer, B., Frank, A., & Ding, C., 2011, arXiv:1112.1710

Cunningham A. J., Frank A., Varnière P., Mitran S., & Jones, T. W. 2009, ApJS, 182, 519

Edgar, R., 2004, New A Rev., 48, 843

Mastrodemos, N., & Morris, M., 1998, ApJ, 497, 303

Makita, M., Miyawaki, K., & Matsuda, T., 2000, MNRAS, 316, 906

Mohamed, S., & Podsiadlowski, P., 2007, Asymmetrical Planetary Nebulae IV

Perets, H. B., & Kenyon, S. J., 2012, arXiv:1203.2918

Soker, N., & Rappaport, S., 2000, ApJ, 538, 241

de Val-Borro, M., Karovska, M., & Sasselov, D., 2009, ApJ, 700, 1148

Witt, A. N., Vijh, U. P., Hobbs, L. M., et al., 2009, ApJ, 693, 1946